

Resonance scattering, absorption and off-centre abundance peaks in clusters of galaxies

J.S. Sanders^{*} and A.C. Fabian

Institute of Astronomy, Madingley Road, Cambridge. CB3 0HA

4 July 2018

ABSTRACT

A possible explanation for the central abundance dips found from spatially-resolved X-ray spectroscopy of several groups and clusters of galaxies is resonance scattering. A number of the prominent iron emission lines are resonance lines. We construct a unique spectral model which takes account of resonance scattering for several thousand resonance lines, projection effects, photoelectric absorption, and allows direct spectral fitting. We apply our model to *Chandra* observations of two clusters with pronounced central abundance dips, Centaurus and Abell 2199. The results show that the effect of resonance scattering on emission from the centre of the cluster can be as much as 30 per cent for the Fe-K resonance lines, and 10 per cent for several Fe-L lines, if turbulence is low. The change to the metallicities obtained by fitting low resolution CCD spectra is at most 10 per cent. Accounting for resonance scattering does not remove the central dip. Allowing for internal absorption within the Centaurus significantly improves the quality of the fits, indicating the presence of absorbing material within the inner 40 kpc of NGC 4696.

Key words: X-rays: galaxies — galaxies: clusters — intergalactic medium

1 INTRODUCTION

Clusters traditionally known as cooling flow clusters, with highly peaked surface brightness profiles and cool cores, typically host a large galaxy in their very centre (Fabian 1994). These galaxies would be expected to pollute their environment with metals, leading to peaked abundance distributions. Such profiles are often seen in X-ray observations of the intracluster medium (ICM) in cooling flow clusters (e.g. Fukazawa et al 1994; De Grandi & Molendi 2001). However some clusters and elliptical galaxies exhibit a dip in abundance in their very centres, including Centaurus (Sanders & Fabian 2002), Abell 2199 (Johnstone et al 2002), Perseus (Sanders et al 2004; Schmidt, Fabian & Sanders 2002; Churazov et al 2003) and NGC 4636 (Jones et al 2002).

Some possible reasons for these abundance dips are resonance scattering (Gilfanov, Syunyaev & Churazov 1987), incomplete spectral modelling (e.g. Buote 2000), a bimodal metallicity distribution (Morris & Fabian 2003), and complex flows (Mathews et al 2003; Fabian 2003).

Resonance scattering in clusters of galaxies was first considered by Gilfanov et al (1987). They pointed out that clusters of galaxies could be optically thick at the energies of strong resonance lines. Resonance transitions are transitions from the ground state of an ion. They are more likely to occur than other transitions as there are a large population of ions in the ground state. If there is a sufficient ion column density along a line-of-sight, radiation which

would otherwise travel to the observer is scattered out of that line-of-sight into another one. As many resonance lines are strong emission lines, this may lead to an underestimate of the abundance of the gas in the centre of the cluster, and an overestimate in the outer parts of the cluster.

We describe here a spectral model which includes the effects of resonance scattering, for use in fitting X-ray spectra from clusters of galaxies. By applying this model to data from clusters exhibiting an off-centre abundance peak we will assess whether resonance scattering can explain these effects. Some authors report that resonance scattering is not important for the bulk of the X-ray emission from the core of the Perseus cluster (Churazov et al 2004; Gastaldello & Molendi 2004). It is however still unclear whether the emission from the very centre of the cluster, or the emission in L-shell lines are significantly affected by resonance scattering.

Several other authors have modelled resonance scattering in clusters, including a Monte Carlo radiative transfer method used on data from M87 (Mathews, Buote & Brighenti 2001), and a radiative transfer method by Shigeyama (1998) in elliptical galaxies. It should also be stated that resonance scattering has been considered important when modelling the solar corona (e.g. Acton 1978).

Rather than a full radiative transfer code, we have aimed for a simpler method which can be calculated in real-time whilst fitting X-ray spectra using XSPEC (Arnaud 1996). We assume the single-scattering approximation, and that photons are conserved. The method calculates the emission and scattering as a function of spectral energy in shells in the cluster. By integrating along lines-of-sight, model X-ray spectra from annuli on the sky are calculated

^{*} E-mail: jss@ast.cam.ac.uk

for a particular temperature, abundance and density cluster profile. The model spectra are fit against data extracted from the appropriate annuli on the sky.

The model can also self consistently account for photoelectrically absorbing material within the cluster. It is interesting to study the amount of this material as it is a possible contributing factor to the lack of emission lines seen emitted from cooling gas (e.g. Fabian et al 2001), although such absorption would need to operate preferentially on the emission from the cool gas.

We assume the solar abundance ratios of Grevesse & Sauval (1998). For distance calculation, we assume that $H_0 = 70 \text{ km s}^{-1} \text{ Mpc}^{-1}$. All uncertainties shown are $1-\sigma$.

2 MODEL

For a particular annulus, the model emission spectrum is calculated by summing the emission from each spherical shell along its line of sight through the cluster. If there are N annuli on the sky, then N shells are used to model the cluster. Each shell is divided into n_s “subshells” to allow for the variation of gas properties across the shell. A typical value of n_s we use is 3. In addition each annulus on the sky is similarly divided into n_s “subannuli”. The spectrum from an annulus is the sum of the spectra from its subannuli.

The electron density, temperature and solar relative abundance are specified at the centre of each shell. The gas properties of subshells are found using linear interpolation in logarithmic radius of the properties from the centres of the nearest shells, or by just using a fixed value within a shell. We later find that using constant values within each shell appears to produce more consistent results.

In general, the model works as follows (Fig. 1). We iterate over each of the subannuli on the sky. For a particular subannulus, we start at the far side of the cluster. We calculate the emission spectrum from the volume of intersection of the outermost subshell with that subannulus. This spectrum is carried forward towards the observer into the volume of intersection with the next subshell. Using the list of resonance lines, we compute how much radiation is scattered as a function of energy in that volume, and remove this radiation from the summed spectrum. The thermal emission from the volume is added to the sum, and the calculation carries on to the next subshell.

To account for radiation scattered into other lines of sight, we keep track of the total radiation scattered by a particular subshell. After we have summed along each line of sight, this spectrum is then distributed among the subannuli according to the fraction expected from Rayleigh scattering.

In addition the model can also take account of X-ray photoelectric absorption within each subshell, applying it consistently. Within each volume of intersection, radiation is removed according to the column density the radiation intercepts. Absorption is also applied to radiation scattered into other lines of sight.

Since the model cluster is spherically symmetric, it is only necessary to do the calculation along one line of sight. We discuss each of the steps of the model in detail below.

2.1 Determination of resonance lines

We used the APED atomic data database (version 1.3.1; Smith et al 2001a) to generate a list of resonance lines to use in the model. This enabled us to use the same source of lines as was used to calculate the emission spectra (APEC; Smith et al 2001b).

For each ion, we identified those lines involving transitions

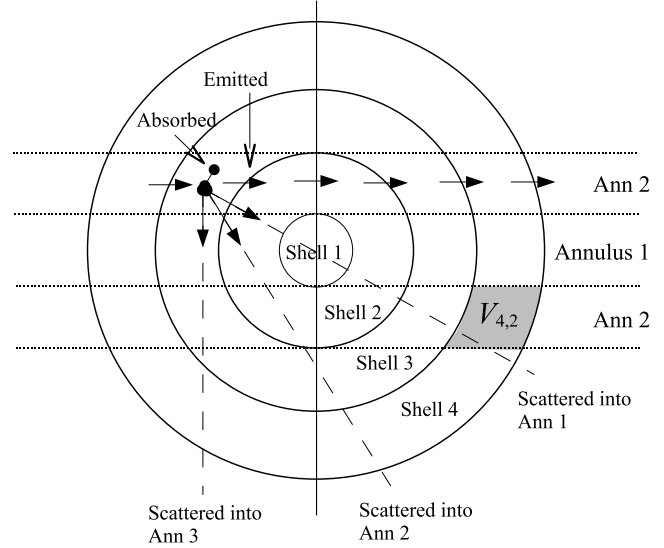


Figure 1. Diagram showing schematics of scattering modelling. This is a cross section of the cluster along the line of sight, with the observer to the right of the diagram. In this example we are looking at the emission summed along the line of sight of annulus 2 (subannuli and subshells are ignored for clarity here).

from the ground state (i.e. the resonance lines). We took their Einstein-A coefficients, A_{ug} , wavelengths, λ , and upper and lower statistical weights for the energy levels the transition is between, g_u and g_g . From these we calculated the oscillator strength of the lines, which in SI units is for each

$$f_{ug} = -\frac{A_{ug} g_u}{3\gamma g_g} \quad (1)$$

where if $\omega_0 = 2\pi c/\lambda$,

$$\gamma = \frac{1}{4\pi\epsilon_0} \frac{2}{3} \frac{e^2}{mc^3} \omega_0^2. \quad (2)$$

In Fig. 2 we show the oscillator strengths of the resonance lines above 0.1 keV and $f_{ug} > 10^{-5}$, identified by element. The relative importance of particular lines will vary with oscillator strength and the abundance of the particular ion, which is a function of temperature. Our model includes all 3574 resonance lines in the APED database, with no oscillator-strength lower threshold.

2.2 Calculation of the emission spectra

If we are fitting spectra from N annuli on the sky, with spectrum a extracted from radii on the sky Π_{a-1} to Π_a , then we fit for the temperature, kT_a , the abundance, Z_a , and the electron density, $n_{e,a}$ at a radius $(\Pi_{a-1} + \Pi_a)/2$ in the cluster, assuming spherical symmetry.

The cluster is modelled by shells in the cluster corresponding to the annuli on the sky. Each shell is divided into n_s subshells (Fig. 3). This gives a total of Nn_s subshells, where n_s is chosen to be as large as possible without making the calculation too slow. Subshell a lies between a radius of R_{a-1} and R_a in the cluster. We use either a fixed temperature, abundance and density in the subshells within each shell, or linear interpolation in logarithmic radius of these values from the centre of each shell. The second option allows for a smooth distribution of gas components between each shell, which we refer to as “interpolation” in this paper. When interpolating, the properties within the inner half of the inner shell

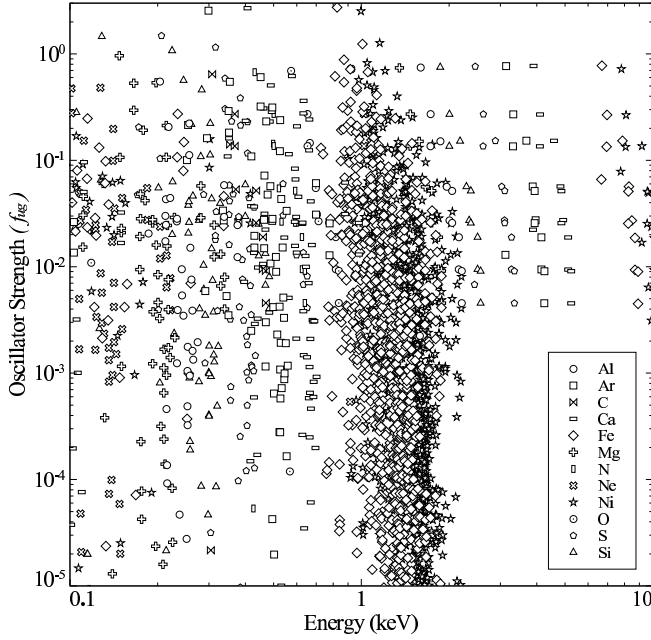


Figure 2. Plot of all the resonance lines above 0.1 keV in APED with an oscillator strength of greater than 10^{-5} .

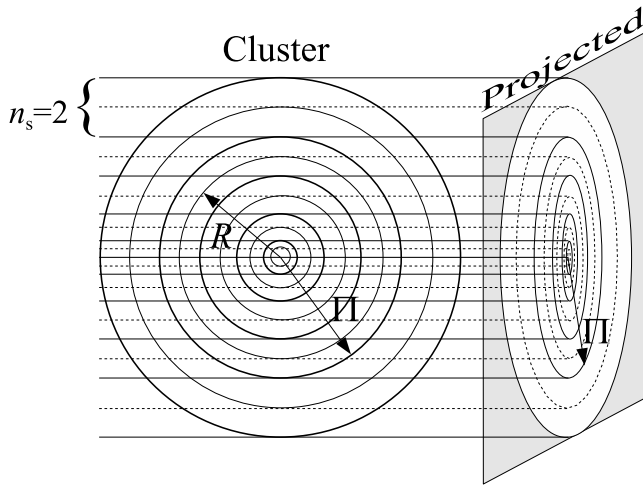


Figure 3. The mapping of the shells and subshells in the cluster, to the annuli and subannuli on the sky. In this example we have 2 subshells and subannuli. Radius Π corresponds to the radii of the annuli on the sky and the shells in the cluster, and radius R corresponds to the radii of the subshells in the cluster.

and the outer half of the outer shell are extrapolated in logarithmic radius from the neighbouring points.

For each subshell, a , in the set of shells we calculate the spectrum of the emitting plasma per unit volume, \mathcal{S}_a , at high spectral resolution in order to adequately sample the major spectral lines over their line width. We used 10^5 linear spectral elements between 0.3 and 9 keV, giving a spectral resolution of 0.087 eV. This is around half the thermal width of a 0.6 keV oxygen line at temperatures of 0.6 keV, or a 1 keV iron line at the same temperature.

The spectrum is calculated using a rewritten implementation of the APEC model in XSPEC, highly optimised for the case of fixed spectral resolution. It works by precalculating high-resolution spectra at the APEC grid-points. The implementation also includes a

Gaussian approximation for the thermal widths of the spectral lines plus an additional turbulence component. The total Doppler width used is (e.g. Mathews et al 2001)

$$\Delta v_D = \frac{v_0}{c} \left(\frac{2kT}{A_{Ewt}m_p} + v_{\text{turb}}^2 \right)^{1/2}, \quad (3)$$

where $v_0 = c/\lambda$ is the central line frequency, A_{Ewt} is the atomic weight of the element producing the line, m_p is the proton mass, and v_{turb} is the turbulent velocity. The line shape is calculated out to three times Δv_D either side of the central frequency.

2.3 Scattering calculation

In addition to the emission spectrum in each subshell, also calculated is the scattering coefficient, κ_a , in units of length^{-1} , over the same energy range and resolution as the emitted spectrum. In order to calculate the scattering coefficient we iterate over each of the resonance lines in the energy range considered. For each line we calculate the scattering profile using (again Mathews et al 2001)

$$\kappa_{\text{line}}(x) = n_H x_{\text{ion}} a_E A_E \left(\frac{e^2}{4\epsilon_0 m_e c} f_{gu} \frac{1}{\pi^{1/2}} \frac{1}{\Delta v_D} \right) e^{-x^2}, \quad (4)$$

where n_H is the hydrogen density of the shell, found using $n_H = n_e/1.2$, A_E is the abundance of the element producing the line relative to solar, a_e is the solar abundance of the element relative to Hydrogen, and x_{ion} is the fraction of the element ionised into the ion producing the line (which is a function of the temperature of the subshell). We use the ionisation fractions of Mazzotta et al (1998), interpolating between the provided values. The dimensionless line frequency, $x = (v - v_0)/\Delta v_D$.

We add the line scattering profile (calculated out to three times Δv_D from the central frequency) to the total ‘scattering coefficient spectrum’ for the subshell, accounting for redshift.

2.4 Calculating the observed spectrum

To model the spectrum in an annulus, we divide the annulus into n_s subannuli (this is chosen to be the same as n_s as was used to create the subshells in Section 2.2, but this need not be the same value). Along the centre of each subannulus, we integrate along the line-of-sight from the back of the cluster to the observer. We take account of the radiation emitted in a particular subshell, and the radiation scattered out of the line-of-sight by that subshell. Optionally, absorbed radiation is also removed. When the spectra for all of the subannuli has been calculated, the code takes the radiation scattered by a particular subshell, computes the fraction scattered into each annulus on the sky, and adds this back to give the final model spectra. Absorption is also optionally applied.

The model for a particular annulus is then computed by summing the integrated spectrum of its subannuli with appropriate area factors. XSPEC fits the model by minimising the sum of the χ^2 or C-statistic of the fits to the individual input spectra.

In detail, the procedure for calculating the emission along each line-of-sight is below, representing spectra as vectors in bold. For subannulus a we sum the emission along its midpoint in radius on the sky, $R_{\text{mid},a} = (R_a + R_{a-1})/2$.

(i) We start with a blank output spectrum, $\mathbf{O}_a \leftarrow \mathbf{0}$, and consider subshell $b = Nn_s$, where the line-of-sight intercepts the cluster on the outer side away from the observer (Fig. 1).

(ii) Take the ‘scattering spectrum’ for the subshell, κ_b , multiply by the line-of-sight length, l_b , between subshell b and $b-1$ at radius on the sky $R_{mid,b}$, to make an ‘optical depth spectrum’, τ_b . To estimate an effective value of l_b we take half the volume between subshell b and $b-1$ intercepting the lines-of-sight between radii on the sky R_a and R_{a-1} , V_{ba} (Fig. 1), and divide by the area on the sky of the subannulus, $A_a = \pi(R_a^2 - R_{a-1}^2)$. V_{ba} is given by the integral,

$$V_{ba} = \int_{y=R_{a-1}}^{R_a} \left(\sqrt{R_b^2 - y^2} - \sqrt{R_{b-1}^2 - y^2} \right) 2\pi y dy. \quad (5)$$

To allow for the fact that the annuli may on the sky may have larger radii than the shells in the cluster, we truncate the integration to where the square-roots are real. This leads to an expression for the volume of

$$V_{ba} = \frac{2}{3} \pi \left[Q(R_{b-1}^2 - R_a^2) - Q(R_b^2 - R_{a-1}^2) + Q(R_b^2 - R_{a-1}^2) - Q(R_b^2 - R_a^2) \right], \quad (6)$$

where

$$Q(x) = \begin{cases} x^{3/2} & : x \geq 0 \\ 0 & : x < 0. \end{cases} \quad (7)$$

We multiply \mathcal{O}_a at each spectral energy by $\exp(-\tau)$ at each spectral energy to take account of the scattering out of the line-of-sight in b ,

$$\mathcal{O}_{a,i} \leftarrow \mathcal{O}_{a,i} \times \exp \left[-\frac{V_{ba}}{A_a} \kappa_{b,i} \right] \text{ for each energy bin, } i. \quad (8)$$

To take account of this radiation being scattered into other lines-of-sight, we keep track of a total spectrum of the radiation which is scattered in subshell b .

(iii) Optionally, absorption within the shell is included in the model. \mathcal{O}_a is multiplied with the result of a PHABS absorber of column density N_H , where $N_H = n_H l_b$, if n_H is the equivalent number of absorbing hydrogen atoms per unit volume, assuming solar abundances.

In detail, the model precalculates the optical depth for unit absorption to improve its speed. In addition the absorption spectrum is stored at lower energy resolution than the rest of the model (we used 8.7 eV energy resolution). This greatly improves the speed of the model. The effect of this simplification to the output spectrum is minimal as the energy dependence of the absorption is smooth, away from the few edges in the spectrum.

(iv) To take account of the emission, we take the emission spectrum per unit volume for subshell b , \mathcal{S}_b , multiply by V_{ba} , and add to the output spectrum

$$\mathcal{O}_{a,i} \leftarrow \mathcal{O}_{a,i} + V_{ba} \mathcal{S}_b \text{ for each } i. \quad (9)$$

(v) Move to the next innermost subshell, i.e. $b \leftarrow b-1$, and go back to (ii). When b is the innermost subshell, iterate over that subshell again, then iterate over increasing b until $b = N_s$. This means that we integrate over the shells on the side of the cluster away from the observer, through the core of the cluster, and out towards the observer to the edge of the cluster again.

The model spectrum for an annulus a is the sum of $\mathcal{O}_{n_s(a-1)}$ to $\mathcal{O}_{n_s a-1}$, plus the contribution of radiation scattered into the line-of-sight.

To calculate the radiation scattered into a line-of-sight, we first take the spectrum of the accumulated radiation which is scattered out of all the lines-of-sight by a particular shell. That spectrum is then divided among the annuli on the sky according to the fraction

Table 1. *Chandra* observations of Centaurus analysed with clean exposure time.

Observation	Observation date	Clean exposure (ks)
504	2000-05-22	21.8
505	2000-06-08	10.0
4954	2004-04-01	80.2
4955	2004-04-02	40.6
5310	2004-04-04	44.1
Total		196.6

of radiation calculated to be scattered into each (see Appendix A). This procedure conserves photon flux, but does not include the physics of the broadening of lines in the scattering process. This effect is irrelevant in the single-scattering assumption unless one is using an instrument which could measure line widths. It is difficult to exactly account for this effect in the current model.

The effects of absorption on the scattered radiation can optionally be accounted for. The model sums up the contribution to the scattered radiation by considering the shells which could scatter into a particular subannulus. Starting from the far side of the cluster, the contribution to the scattered spectrum is calculated for the outermost half-subshell. This radiation is carried to the half-subshell next nearest the observer, absorption is applied within this subshell, and the scattered contribution added. We repeat this process until we reach the half-subshell nearest the observer.

After generating the high resolution model spectra, they are downsampled to instrument resolution for spectral fitting in XSPEC.

3 APPLICATION OF MODEL

3.1 Centaurus cluster

We applied our model to the Centaurus cluster which has a clear abundance drop in its centre (Sanders & Fabian 2002; Fabian et al 2005). The details of the observations analysed are shown in Table. 1, and are the same observations as discussed in Fabian et al (2005). Each of the observations were taken using the ACIS-S3 back-illuminated CCD. The LC_CLEAN tool was used to filter periods with flares, using the lightcurve of the ACIS-S1 back-illuminated CCD in the band 2.5 to 7 keV, yielding a total exposure of 196.6 ks. Each of level-1 event files for the observations were reprocessed using the PSU CTI corrector (Penn State University corrector for charge transfer efficiency), version 1.45, (Townsley et al 2002a,b). Blank sky background files were used during spectral fitting. The exposure times of the background event files were modified to ensure the same count rate as the observations in the 9 to 12 keV band (where background dominates over source counts). We used a response matrix generated using the PSU ACIS CCD simulator, using an energy resolution of 4 eV. Ancillary response matrices were created using the CIAO MKWARF tool (CIAO version 3.2.2) and the PSU QEU file, weighting the spatial regions using the 0.5 to 7.0 keV band. Background spectra were extracted from the same spatial region in blank-sky event files.

We analysed the cluster in two spatial parts. Our previous work showed that the eastern and western halves are distinct. There is a plume-like feature in the eastern central regions. Therefore we concentrated on the western half, where the central regions show less disturbance. Fig. 4 shows the regions used in this analysis. As the different datasets examined were taken with different roll-

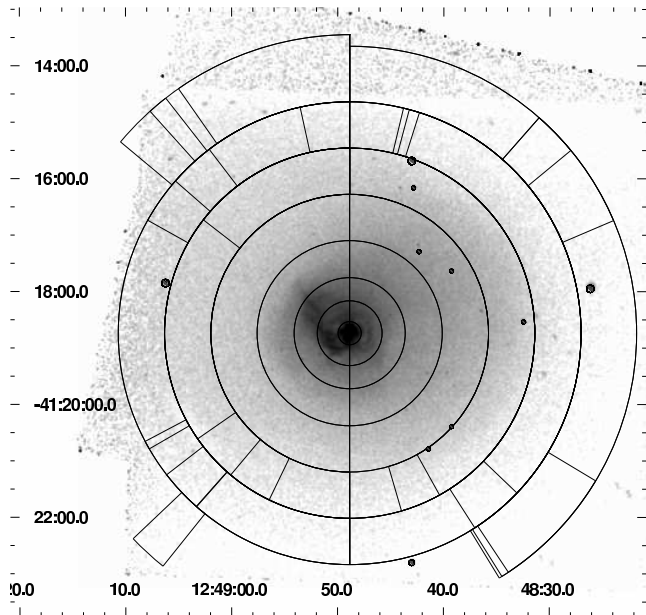


Figure 4. Regions used for spectral fitting. The image is exposure map corrected, and smoothed by a Gaussian of 1 arcsec. The western half of the cluster is least disturbed in the central regions.

angles and aim-points, the starting and stopping angles of the sectors were modified for each dataset to fit on the S3 CCD.

We fit the spectra in XSPEC using our resonance scattering model, fitting the datasets simultaneously, and minimising the χ^2 during the fit. The spectra were fit between 0.5 and 7 keV, with the spectra grouped to have a minimum of 20 counts per spectral bin. A PHABS (Balucinska-Church & McCammon 1992) component was used to account for Galactic absorption, applied equally to each annulus. The absorption column density of this component was allowed to be free in the fits.

In Fig. 5 we show the results of the spectral fits for the western and eastern half of the cluster using a variety of variants on the resonance scattering model. The points plotted show the model optionally including the effects of resonance scattering, interpolation of the gas properties to smooth the profile, and fitting for internal absorption within the cluster. The quality of the fits are shown in Table 2. We also calculated the profiles using radial bins with half the width in the Western half of the cluster (Fig. 6).

Accounting for resonance scattering improves the quality of the spectral fits slightly. Allowing multiple interpolated components per shell and allowing for internal absorption improves the fits much more.

It can be seen, as we will discuss later, that the effect on the derived abundance including resonance scattering is generally small. Greater changes to the metallicities are found using models which interpolate the gas properties across each shell. However the interpolation feature seems to exacerbate instabilities in the spectral fit. This is particularly evident in the outer regions of the temperature profile of the eastern half. To gauge whether the interpolation technique improves the accuracy of the results, the lower spatial resolution interpolated and non-interpolated results can be compared with those using higher spatial resolution (Fig. 6). Those profiles from models which do not interpolate the gas properties appear to be consistent. Interpolated models produce inconsistent results, suggesting that the assumption of spherical symmetry is inadequate, or there is additional non-projected multiphase material. The second

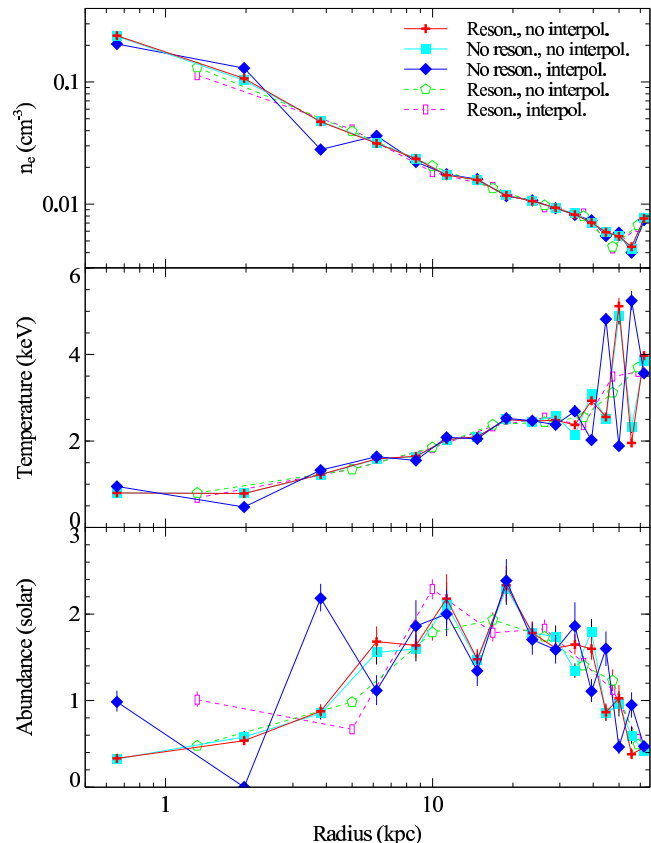


Figure 6. Profiles for the Western half of Centaurus using radial bins with half the width. Overplotted in hollow symbols are results from Fig. 5 including and not including interpolation of the gas properties.

most important factor appears to be modelling absorption, which we discuss separately in Section 3.3.

To quantify the effect that the resonance scattering model is having on the spectrum, we show in Fig. 7 the fractional difference between the best fitting non-interpolated resonance scattering model, and that model with resonance scattering disabled. In the innermost shell the maximum effect on Fe-K lines is around 30 per cent, and around 10 per cent for the Fe-L lines. The overall trend is what is naively expected: Fe-L is scattered out of the cooler inner shells into outer shells, but Fe-K is scattered out of the hotter outer shells into the inner shells (see Fig. 8 for detail).

We also carried out spectral fitting with an additional 300 km s^{-1} turbulent velocity component. The results from these fits lay between the results without resonance scatter, and with resonance scattering, as would be expected.

The optical depth of the scattering (ignoring radiation scattering back into the line of sight) is around 1.3 for one of the Fe-K lines, if we examine the radiation emitted from the centre of the cluster. A few of the Fe-L lines approach optical depths of unity. The probability of these photons being scattered again is in fact smaller than a naive calculation would give, as the lines are broadened by the scattering. The single scattering approximation is justified by this.

3.2 Abell 2199

We also applied our model to Abell 2199, which was found to have an abundance drop by Johnstone et al (2002). A2199 is a rich clus-

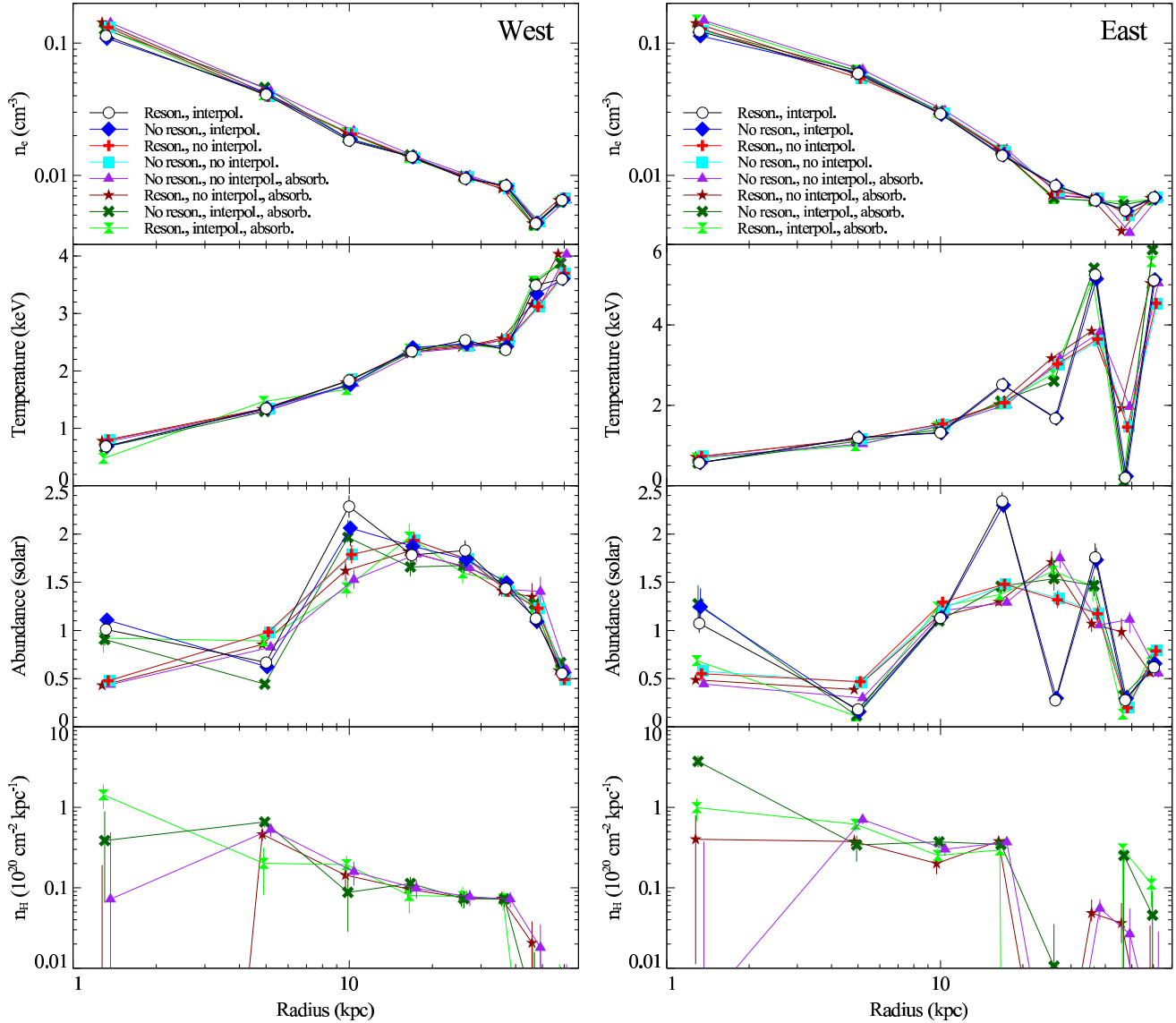


Figure 5. Radial electron density (top), temperature, abundance, and internal photoelectric absorption (bottom) profiles for the west (left) and east (right) of the Centaurus cluster. Each symbol and line shows the profile with a variant of the model. “Reson.” indicates a model including the effects of resonance scattering and “interpol.” uses a smooth range of components (5 in west and 3 in east) within each shell. “absorb.” indicates that internal absorption is fitted for within the cluster. The radius marked is the mean radius of each shell. The points have been offset from the black circle slightly horizontally for clarity.

ter of galaxies at a redshift of 0.0309. The cluster has a temperature of 4.7 keV (Edge & Stewart 1991), and a peaked surface brightness profile.

We examined spectra extracted from *Chandra* observations 497 and 498, yielding a total exposure of 33.3 ks after removal of flares. The same regions for spectral extraction as were used by Johnstone et al (2002) for their results including projection effects, were chosen. The event files were reprocessed with the latest appropriate gain files in CALDB 3.01. We used blank-sky fields for background subtraction. We minimised the χ^2 statistic during the spectral fitting, and fitted the data between 0.5 and 7 keV. Again, we accounted for Galactic absorption with a free PHABS component. We did not use the PSU CTI corrector on this dataset as the one of the observations was taken before the date the corrector is valid from.

In Fig. 9 are shown the radial profiles from the results of our spectral fitting, showing the results accounting for resonance scat-

Table 3. Effect on the quality of the spectral fit for A2199, when including resonance scattering. There is virtually no change to the quality of the fit, although the fit including resonance scattering is slightly better.

Resonance scattering	χ^2	dof	Reduced χ^2
No	4113.9	3694	1.11
Yes	4105.8	3694	1.11

tering and without. Again we see that the effect of including resonance scattering in the model is small on the measured abundances.

3.3 Absorption

If only Galactic absorption is assumed, there is evidence for low energy residuals in the fits to the inner region of the eastern half of the Centaurus cluster. This may be indicating that there is pho-

Table 2. Quality of fits for the various models and data for Centaurus. The sectors used are West, the West with finer sectors (half the width of the normal sectors), and East. If resonance scattering is indicated, then resonance scattering was modelled (with no turbulence). Interpolation specifies whether the properties of the gas were interpolated within the subshells (5 for thick sectors, west, 3 for others). The absorption column indicates whether internal photoelectric absorption was modelled within the cluster.

Sector	Resonance scattering	Interpolation	Absorption	χ^2	dof	Reduced χ^2
West	No	No	No	13039	9533	1.37
West	Yes	No	No	13005	9533	1.36
West	No	Yes	No	12938	9533	1.36
West	Yes	Yes	No	12868	9533	1.35
West	No	No	Yes	12613	9525	1.32
West	No	Yes	Yes	12511	9525	1.31
West	Yes	No	Yes	12626	9525	1.33
West	Yes	Yes	Yes	12417	9525	1.30
West (fine)	No	No	No	18735	15252	1.23
West (fine)	Yes	No	No	18651	15252	1.22
West (fine)	No	Yes	No	18591	15252	1.22
East	No	No	No	13525	8774	1.54
East	Yes	No	No	13439	8774	1.53
East	No	Yes	No	12989	8774	1.48
East	Yes	Yes	No	12797	8774	1.46
East	No	No	Yes	12576	8766	1.43
East	No	Yes	Yes	12503	8766	1.43
East	Yes	No	Yes	12700	8766	1.45
East	Yes	Yes	Yes	12509	8766	1.43

toelectrically absorbing material in that region. There is also evidence for small spatial scale absorbing material in the central regions of the cluster with a similar morphology to the dust lane in NGC 4696 (Crawford et al 2005). The Centaurus *Chandra* data are of such high quality that we are able to test for the presence of an absorbing component within the cluster for both sectors. Allow for absorption within each shell obtains measurements for the amount of absorbing material per unit volume shown in the bottom panel of Fig. 5.

The amount of absorption found in the western half of Centaurus appears fairly consistent between the model variants, except perhaps in the very innermost annulus. The level of absorption appears to increase inside 40 kpc radius, in the form of a rough power law. The region with the apparent absorbing material appears to be only that gas below around 2.5 keV. The minimum value of $0.08 \times 10^{20} \text{ cm}^{-2} \text{ kpc}^{-1}$ within the inner 40 kpc, would indicate an equivalent absorbing hydrogen density of $3 \times 10^{-3} \text{ cm}^{-3}$. Within 40 kpc this would correspond to a mass of $2 \times 10^{10} M_{\odot}$ of absorbing material assuming solar relative abundances.

We should note, however, that there is a build-up of contaminant on the ACIS detector, which is not spatially uniform (see Sanders et al 2004 for a map of this contaminant from a Perseus cluster observation). Although the MKWARF tool that we used to create the ancillary responses includes a correction for the spatial variation of this contaminant over time, there may still be uncertainties in this calibration. It is possible that the evidence we show is due to calibration uncertainties. The absorbing material on small spatial scales found by Crawford et al (2005) indicates that the calibration is not likely to be responsible for all of the signal within the central regions. It will be important to confirm the absorption detection in data from *XMM-Newton* in future.

4 DISCUSSION

4.1 Resonance scattering

Our model shows that the effect of resonance scattering in the two clusters of galaxies examined is minimal to the determination of abundances from CCD resolution X-ray spectra. The change in abundance measured is less than 10 per cent. The model assumes that spherical symmetry is a good approximation in these clusters. It also ignores the effects of non-Solar abundance ratios, or the presence of multiphase gas which is not the result of projection.

The largest effect on the determined abundance in the central regions is using a model which allows for an interpolated range of components in each shell. Although this should produce results which more closely match the real profile if the gas properties vary smoothly, it seems that it is prone to effects which cause instability and oscillating profiles (e.g. in the outer parts of the eastern temperature profile, the western profile at high spatial resolution; Fig. 6, and the inner region of the eastern abundance profile). We suspect that non-spherical geometry may be a cause of this instability. The inner parts of the cluster show obvious asymmetric features. The cluster, centred on NGC 4696, is also thought to be merging or has merged with a subcluster 15 arcmin to the east centred on NGC 4709 (Allen & Fabian 1994; Churazov et al 1999; Furusho et al 2001; Dupke & Bregman 2001). The oscillations are particularly evident in the outer regions on the eastern sector.

Although resonance scattering appears not to be important when examining low spectral resolution spectra from clusters of galaxies (at least in clusters similar to Centaurus), it is an important process when examining high resolution X-ray cluster spectra in detail. The effect increases the strength of the Fe-K resonance lines by up to 30 per cent from the centre of the Centaurus cluster if turbulence can be neglected. The effect on Fe-L resonance lines is smaller (< 10 per cent), but there are many more of them. When fitting the low resolution CCD spectra from *Chandra* the effect on the obtained abundance is small (< 10 per cent). However, if turbulence is low the effect will be important to consider when exam-

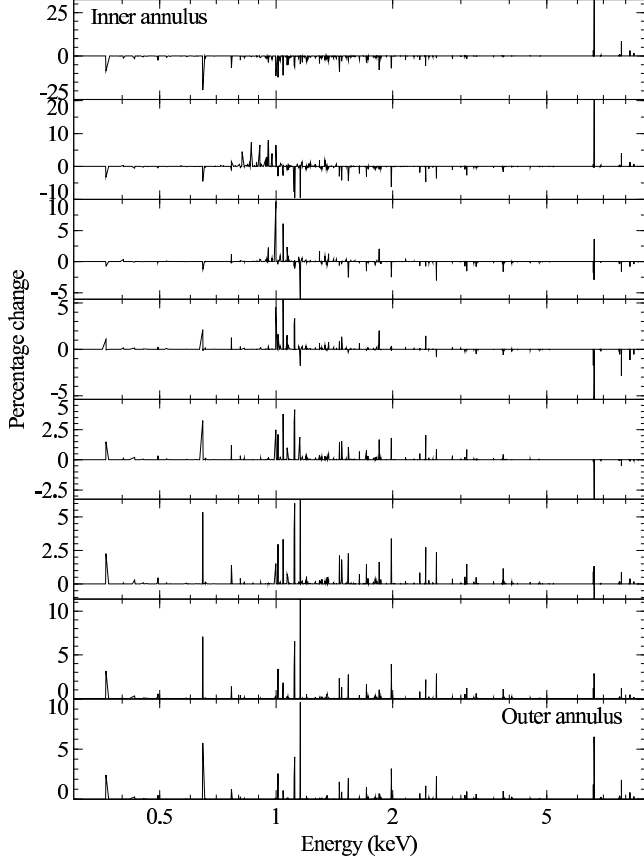


Figure 7. Fractional difference between the best fitting resonance scattering model spectrum for the western half of the Centaurus cluster (Fig. 5 left), and with the model with resonance scattering disabled. Here a model without absorption or interpolation was used. A positive value shows more emission in the resonance scattering model. The top panel shows the results for the innermost shell, and the bottom the outermost shell. No turbulent velocity components are included here.

ining high spectral resolution data. The straightness of the $H\alpha$ filaments in the Perseus cluster suggests that the intracluster medium may not be highly turbulent (Fabian et al 2003), although gas flows ~ 100 s km s^{-1} are inevitable. It will be useful to include resonance scattering effects when examining higher resolution spectra from the *XMM-Newton* Reflection Grating Spectrometers, or from a future X-ray bolometer mission.

4.2 Photoelectric absorption

Photoelectric absorption affects the spectra emitted from the innermost regions of clusters of galaxies, as is indicated by the small scale variations in NGC 4696 (Crawford et al 2005). We find evidence for larger scale absorbing material in Centaurus, providing calibration uncertainties are not important. If this absorbing material can preferentially act on the radiation from cool material, it has the possibility of disguising the rate of cooling in the cluster (Fabian et al 2001).

4.3 Off centre abundance peaks

Our results show that accounting for projection, resonance scattering and absorption does not remove the abundance drop seen in the

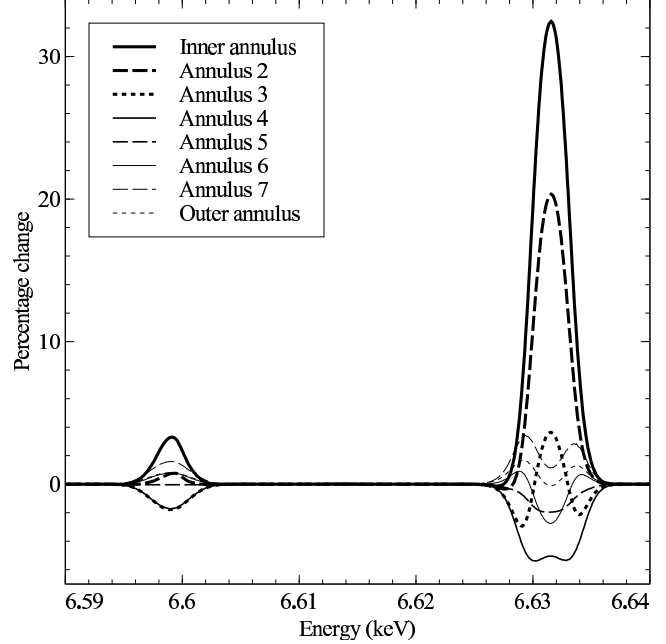


Figure 8. Detail of Fig. 7 around the Fe-K lines. Positive values means that the resonance scattering model predicts more emission from the shell than simple projection.

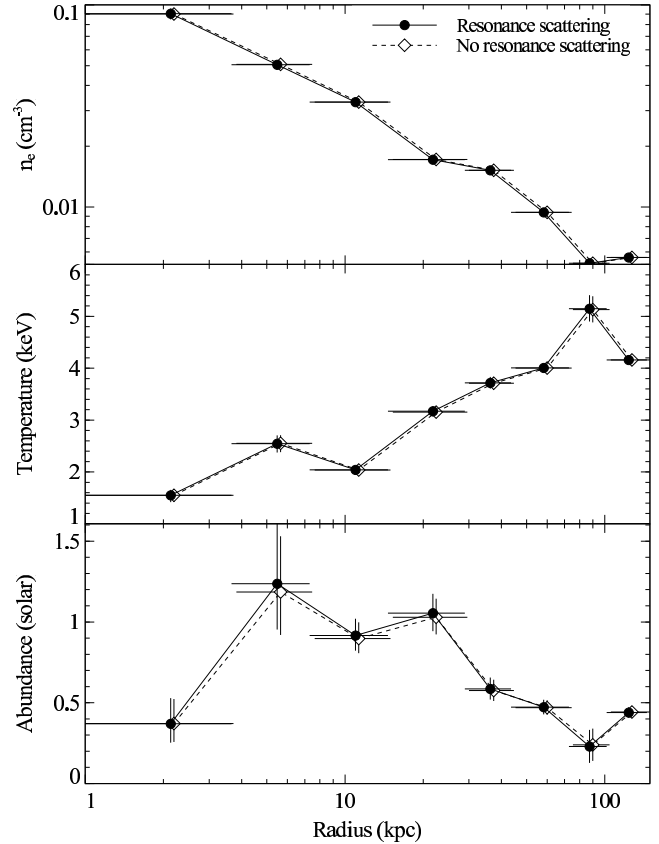


Figure 9. Density, temperature and abundance profiles for Abell 2199. Shown are the results including resonance scattering effects, and not including such effects. No subshell interpolation was used in these results. The results without resonance scatter have been offset horizontally for clarity.

centre of the Centaurus cluster. Unfortunately this result is not as clear cut as we would like.

We have shown that when fitting projected spectra, allowing for extra absorption, and using three temperature components, it is possible to lose the drop in the central metallicity (Fabian et al 2005). The uncertainty on the innermost gas abundance does however, increase substantially, which means the drop may or may not exist.

We have also tried fitting models accounting for projection, but using two temperature components in each shell. In the fits the O, Ne, Mg, Si, S, Ar, Ca, Fe and Ni metallicities are allowed to vary, while the others are fixed at solar. Both of the temperature components are constrained to have the same metallicities. Fig. 10 shows the results using the APEC and MEKAL (Mewe, Gronenschild & van den Oord 1985; Kaastra 1992; Liedahl, Osterheld & Goldstein 1995) spectral models for the components. It should be noted that the MEKAL results used the updated version of the MEKAL code which is available in SPEX (Kaastra 2000). We discuss this further in Sanders & Fabian (in preparation), where we will also examine the relative abundances in more depth, in the context of models of enrichment.

The plots show that there are declines in metallicity in many elements, even with this fairly complex model. The declines are not as deep as for single temperature projected models, however. If there is additional absorption within the central region (as we may have detected), or additional temperature components which do not have spherical symmetry, then this could remove the drop. We have also tried simple single-temperature models, but including a nonthermal component in the innermost bins, but this was insufficient.

Although the drop in Centaurus may be removed with a complex enough spectral model, it is more difficult to remove the decline seen in the Perseus cluster, for which we have done detailed spatial mapping (Sanders et al 2004; Sanders, Fabian & Dunn 2005). This drop has a large spatial extent, and the distribution of the metals within the ICM appear to have a great deal of structure. It may be possible that the inclusion of a range of detected multiphase gas (Fabian et al 2006), and nonthermal emission (Sanders et al 2005), may help remove the drop, but our initial results indicate that they do not. The relative amount of cool gas in the Perseus cluster is much smaller than Centaurus, compared to the hotter gas. Unfortunately it is impossible to properly account for projection in Perseus due to the complex nature of the cluster core. We therefore conclude that there is much scope for further research into the distribution of the metals found in cluster cores.

MODEL AVAILABILITY

The model is available for download from <http://www-xray.ast.cam.ac.uk/papers/reson/>

ACKNOWLEDGEMENTS

We would like to thank R. Smith for help in using APED and APEC. ACF acknowledges the support of the Royal Society.

APPENDIX A: SCATTERING INTO THE LINE-OF-SIGHT

Resonant scattering is not isotropic for $j = 0$ and $\Delta j = 1$ transitions but has a Rayleigh (dipole) phase function (Hamilton 1947), with

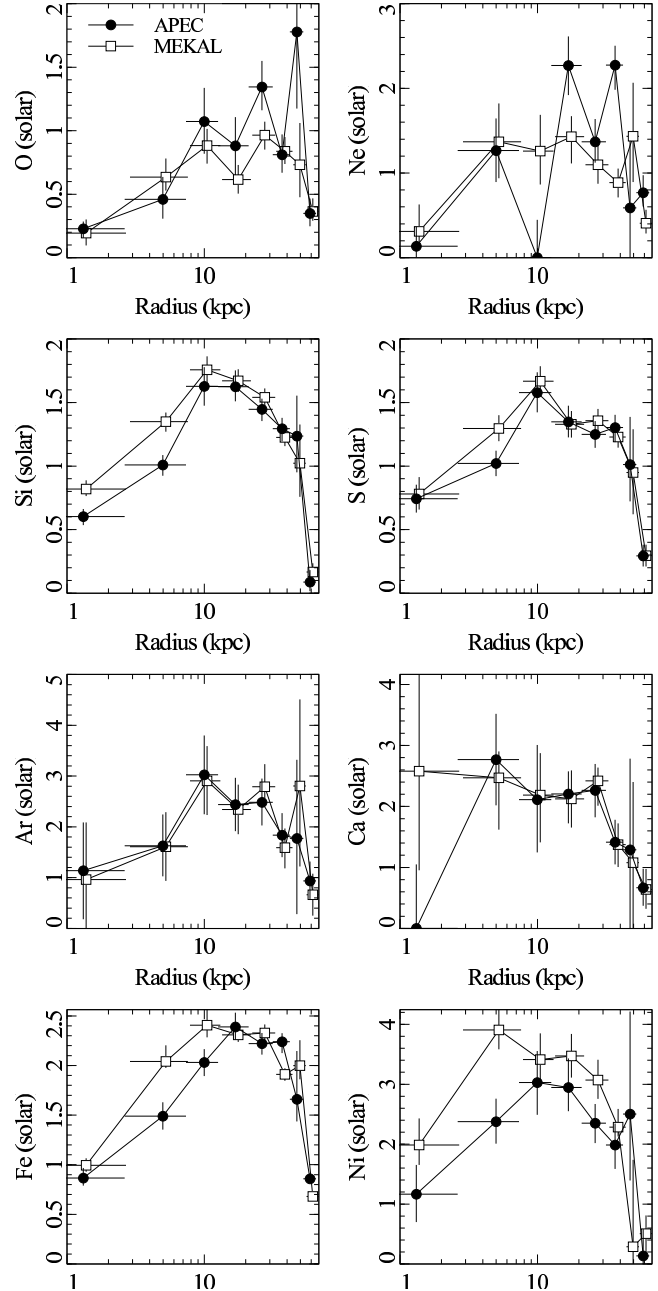


Figure 10. Best fitting metallicities for the western half of the cluster when fitting models including projection, using two temperature components in each annulus. APEC and MEKAL models are compared, with the MEKAL results slightly offset in radius for clarity.

the form

$$\psi(\theta) = \frac{3}{4} (1 + \cos^2 \theta), \quad (\text{A1})$$

which is normalised to 4π when integrated over all solid angle. Other resonance scattering transitions can be isotropic in nature, or a combination of dipole and isotropic.

We assume a Rayleigh phase function in our calculations, which is true for many important resonance lines. The choice of phase function, however, makes little difference to the distribution of the surface brightness on the sky (Sazonov, Churazov & Sunyaev 2002), as shown in our simulation below.

If we assume the photons being scattered are travelling in ra-

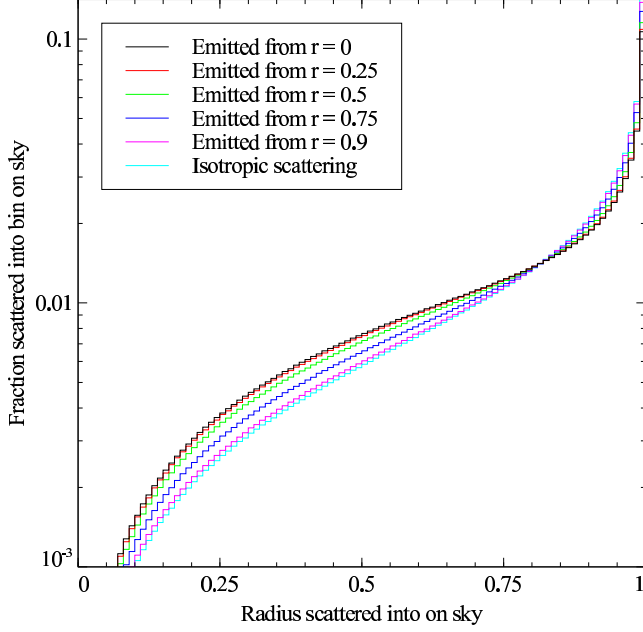


Figure A1. Distribution of light on the sky (in 100 bins) for photons randomly emitted isotropically in a system from fixed radii, r , but scattered by a thin shell at $r = 1$. All of these results assume Rayleigh scattering, except for the labelled isotropic case. As the emitter moves closer to the scatterer, the dipole scattering becomes more like isotropic scattering. Note that most of the flux is scattered beyond $r = 0.75$ in all cases.

dial directions before scattering, then the fraction of photons scattered from a shell of radius R_1 to R_2 into an annulus on the sky of radius A_1 to A_2 is

$$f_{\text{scat}}(R_1, R_2, A_1, A_2) = \frac{1}{\frac{4}{3}\pi(R_2^3 - R_1^3)} \frac{1}{4\pi} \int_{r=R_1}^{R_2} \int_{\phi=0}^{2\pi} \left[\int_{\theta=\sin^{-1}\frac{A_1}{r}}^{\sin^{-1}\frac{A_2}{r}} \frac{3}{4} (1 + \cos^2\theta) \sin\theta d\theta + \int_{\theta=\pi-\sin^{-1}\frac{A_1}{r}}^{\pi-\sin^{-1}\frac{A_2}{r}} \frac{3}{4} (1 + \cos^2\theta) \sin\theta d\theta \right] d\phi r^2 dr, \quad (\text{A2})$$

assuming that equal photons are scattered by equal volume in the scattering shell. When integrated this becomes

$$f_{\text{scat}}(R_1, R_2, A_1, A_2) = \frac{1}{4(R_1^3 - R_2^3)} \left[(4R_1^2 - 7A_1^2) \sqrt{R_1^2 - A_1^2} + (7A_1^2 - 4R_2^2) \sqrt{R_2^2 - A_1^2} + (7A_2^2 - 4R_1^2) \sqrt{R_1^2 - A_2^2} + (4R_2^2 - 7A_2^2) \sqrt{R_2^2 - A_2^2} + 3A_1^3 \left(\sin^{-1}\frac{A_1}{R_2} - \sin^{-1}\frac{A_1}{R_1} \right) + 3A_2^3 \left(\sin^{-1}\frac{A_2}{R_1} - \sin^{-1}\frac{A_2}{R_2} \right) \right]. \quad (\text{A3})$$

If the scatterer is close to the the source of the photons then this calculation is not accurate. To examine the magnitude of this effect, we have performed Monte Carlo simulations of individual photons. We simulated sets of 10^8 photons emitted at five different radii in cluster, but scattered at the same radius, for both dipole and isotropic scattering. Fig. A1 plots the average distribution on the sky of the scattered radiation from these simulations. The results from Equation A3 are exactly the same as those from the simulation when the light is emitted from $r = 0$ with Rayleigh scattering.

Isotropic scattering shows no change in the distribution as the emitter moves closer to the scatterer. We therefore only plot a single line for that phase function. For dipole scattering, as the emitter approaches the scatterer, the distribution becomes more like an isotropic scatterer. There is little change in the shape of the distribution until the emitter is $3/4$ of the radius of the scatterer. As they get closer, the majority of the flux is scattered towards slightly smaller radii. Note that the magnitude of the effect on the sky is small. It is magnified by the logarithmic scale used in the plot, which is necessary to show it.

As the effect of the emitter moving towards the scatterer is relatively small, and the choice of phase function is small too (also see Sazonov et al 2002), we assume Equation A3 in our calculations.

REFERENCES

- Acton L.W., 1978, *ApJ*, 225, 1069
 Allen S.W., Fabian A.C., 1994, *MNRAS*, 269, 409
 Arnaud K.A., 1996, *Astronomical Data Analysis Software and Systems V*, eds. Jacoby G. and Barnes J., p17, ASP Conf. Series volume 101
 Balucinska-Church M., McCammon D., 1992, *ApJ*, 400, 699
 Buote D.A., 2000, *ApJ*, 539, 172
 Cash W., 1979, *ApJ*, 228, 939
 Churazov E., Gilfanov M., Forman W., Jones C., 1999, *ApJ*, 520, 105
 Churazov E., Forman W., Jones C., Böhringer H., 2003, *ApJ*, 590, 225
 Churazov E., Forman W., Jones C., Sunyaev R., Böhringer H., 2004, *MNRAS*, 347, 29
 Crawford C.S., Hatch N.A., Fabian A.C., Sanders J.S., 2005, *MNRAS*, 363, 216
 De Grandi S., Molendi S., 2001, *ApJ*, 551, 153
 Dupke R., Bregman J.S., 2001, *ApJ*, 562, 266
 Edge A.C., Stewart G.C., 1991, *MNRAS*, 252, 414
 Fabian A.C., 1994, *A&AR*, 32, 277
 Fabian A.C., Mushotzky R.F., Nulsen P.E.J., Peterson J.R., 2001, *MNRAS*, 321, L20
 Fabian A.C., 2003, *MNRAS*, 344, L27
 Fabian A.C., Sanders J.S., Crawford C.S., Conselice C.J., Gallagher III J.S., Wyse R.F.G., 2003, *MNRAS*, 344, L48
 Fabian A.C., Sanders J.S., Taylor G.B., Allen S.W., 2005, *MNRAS*, 360, L20
 Fabian A.C., Sanders J.S., Taylor G.B., Allen S.W., Crawford C.S., Johnstone R.M., Iwasawa K., 2006, *MNRAS*, in press, astro-ph/0510476
 Fukazawa Y., Ohashi T., Fabian A.C., Canizares C.R., Ikebe Y., Makishima K., Mushotzky R.F., Yamashita K., 1994, *PASJ*, 46, L55
 Furasho T., et al., 2001, *PASJ*, 53, 421
 Gastaldello F., Molendi S., 2004, *ApJ*, 600, 670
 Gilfanov M.R., Syunyaev R.A., Churazov E.M., 1987, *Soviet Astr. Lett.*, 13, 3
 Grevesse N., Sauval A.J., 1998, *Space Sci. Rev.*, 85, 161
 Hamilton D.R., 1947, *ApJ*, 106, 457
 Johnstone R.M., Allen S.W., Fabian A.C., Sanders J.S., 2002, *MNRAS*, 336, 299
 Jones C., Forman W., Vikhlinin A., Markevitch M., David L., Warmflash A., Murray S., Nulsen P.E.J. 2002, *ApJ*, 567, L115
 Kaastra J.S., 1992, *An X-Ray Spectral Code for Optically Thin Plasmas* (Internal SRON-Leiden Report, updated version 2.0)
 Kaastra J.S., 2000, in M.A. Bautista, T.R. Kallman, A.K. Pradhan, eds, *Atomic Data Needs for X-ray Astronomy*, <http://heasarc.gsfc.nasa.gov/docs/heasarc/atomic/>, 161
 Liedahl D.A., Osterheld A.L., Goldstein W.H., 1995, *ApJ*, 438, L115
 Mathews W.G., Buote D.A., Brighenti F., 2001, *ApJ*, 550, L31
 Mathews W.G., Brighenti F., Buote D.A., Lewis A.D., 2003, *ApJ*, 596, 159
 Mazzotta P., Mazzitelli G., Colafrancesco S., Vittorio N., 1998, *A&AS*, 133, 403

- Mewe R., Gronenschild E.H.B.M., van den Oord G.H.J., 1985, *A&AS*, 62, 197
- Morris R.G., Fabian A.C., 2003, *MNRAS*, 338, 824
- Sanders J.S., Fabian A.C., 2002, *MNRAS*, 331, 273
- Sanders J.S., Fabian A.C., Allen S.W., Schmidt R.W., 2004, *MNRAS*, 349, 952
- Sanders J.S., Fabian A.C., Dunn R.J.H., 2005, *MNRAS*, 360, 133
- Sazonov S.Y., Churazov E.M., Sunyaev R.A., 2002, *MNRAS*, 333, 191
- Schmidt R.W., Fabian A.C., Sanders J.S., 2002, *MNRAS*, 337, 71
- Shigeyama T., 1998, *ApJ*, 497, 587
- Smith R.K., Brickhouse N.S., Liedahl D.A., Raymond J.C., 2001a, *Spectroscopic Challenges of Photoionized Plasmas*, ASP Conference Series Vol. 247, eds Gary Ferland and Daniel Wolf Savin. San Francisco: Astronomical Society of the Pacific, p161
- Smith R.K., Brickhouse N.S., Liedahl D.A., Raymond J.C., 2001b, *Astrophysical Journal*, 556, L91
- Townsley L.K., Broos P.S., Chartas G., Moskalenko E., Nousek J.A., Pavlov G.G., 2002, *Nuc. Instr. and Meth. in Phys. Res. A*, 486, 716
- Townsley L.K., Broos P.S., Nousek J.A., Garmire G.P., 2002, *Nuc. Instr. and Meth. in Phys. Res. A*, 486, 751